Check for updates

Sunlight light-driven degradation of anthracene and naphthalene on robust Cu^{2+}doped ZnO nanoparticles from simulated rainwater: optimization factors, kinetics, and reusability†

Meenu,[a] Manviri Rani[*a] and Uma Shanker [ID] [*b]

This research investigated the detection and removal of priority polycyclic aromatic hydrocarbons (PAHs) from metropolitan rainwater runoff through photocatalytic degradation. The ubiquitous distribution of PAHs in all environment matrices has gained scientific interest because of the risk for the security of drinking water which is a growing concern to the next generation worldwide. Anthracene and naphthalene are primarily used in the petrochemical, chemical, and food industries and are suspected to have carcinogenic and persistent properties and have been detected in rainwater runoff. Herein, a Cu doped ZnO nanocomposite is green synthesized *via* facile precipitation and used for photodegradation of NAP and ANT in simulated rainwater under natural light exposure. Sharp PXRD peaks confirmed that the spherical nanocomposite had great crystallinity and purity. XPS analysis, PXRD, and FE-SEM confirmed the effective doping of Cu with ZnO. Following this, under various reaction conditions (pollutant: 10–60 mg L^{-1}; catalyst: 2–12 mg; pH: 3–9, dark sunlight, humic acid, and chloride ion: 0.1–1 M), the Cu@ZnO nanocomposite was assessed for the efficient removal of NAP and ANT. Cu@ZnO displayed maximum degradation of NAP (96%) and ANT (94%) at 10 mg L^{-1} conc. of each PAH with a 10 mg catalytic dose at neutral pH in the presence of direct sunlight. First-order kinetics followed by initial Langmuir adsorption constituted the degradation process. The efficiency of green fabricated Cu@ZnO for the removal of NAP and ANT in real rainwater samples was analyzed by HPLC. Predominant reactive species and safer metabolite formation in the photocatalysis process of PAHs were studied by scavenger and GC-MS analysis. The reusability of the nanocomposite up to nine cycles demonstrated the remarkable sustainability and cost-effectiveness of the nanocomposite. Thus, the Cu@ZnO nanocomposite has good catalytic properties for pollutant remediation, and industrial and other applications in laboratory control as well as real systems.

Environmental significance

Polycyclic aromatic hydrocarbons (PAHs) are ubiquitous pollutants released from natural and anthropogenic activities like petrochemical effluent, oil spills, and industrial effluent found particularly in rainwater runoff, causing toxicity, persistence, and bioaccumulation. PAHs, like naphthalene (NAP) and anthracene (ANT), are hazardous by-products of coal and petroleum industries and are primarily consumed by humans through direct contact with polluted water, diet, and inhalation. ANT and NAP are crucial models for PAH degradation studies due to their structural similarities with carcinogenic and mutagenic PAHs. These low molecular weight compounds have high water solubility, making them potential water system contaminants. PAHs are carcinogenic even at low concentrations and resistant to biological and chemical degradation, prompting research for efficient remediation strategies. This work investigates the green synthesis (*Azadirachta indica* as a surfactant and reducing agent) of a Cu-doped ZnO nanocomposite *via* facile precipitation, which is used for photodegradation of NAP and ANT in simulated rainwater under natural light exposure. The synthesized nanocomposite demonstrated excellent surface activity and was reusable for up to nine consecutive cycles, making it a promising solution for various applications, including heterogeneous catalysis, electrochemistry, optics, and environmental remediation.

aDepartment of Chemistry, Malaviya National Institute of Technology Jaipur, Jaipur 302017, Rajasthan, India. E-mail: manviri.chy@mnit.ac.in; Tel: +91- 9549-650-291

bDepartment of Chemistry, Dr B R Ambedkar National Institute of Technology Jalandhar, Office Number-107, Jalandhar 144008, Punjab, India. E-mail: shankeru@nitj.ac.in; umaorganic29@gmail.com; Tel: +91- 7837-588-168

1. Introduction

Polycyclic aromatic hydrocarbons (PAHs) are typical kinds of POPs found in the environment, exhibiting toxicity, environmental persistence, and possible bioaccumulation.[1] PAHs are primarily released from natural and anthropogenic activities,

© 2024 The Author(s). Published by the Royal Society of Chemistry

Environ. Sci.: Adv., 2024, **3**, 249–265 | **249**

such as petrochemical effluent, oil spills, and industrial effluent (Fig. 1S†). The main source of PAHs is the incomplete combustion of crude oil and fossil fuels, motor vehicle emissions, asphalt road surfaces, vehicle tire wear, petrochemical industry effluent, and accidental oil spills.[2] PAHs, such as naphthalene (NAP) and anthracene (ANT), are hazardous by-products of coal and petroleum industries.[3] PAHs enter ecosystems through industrial activities, particularly in rainwater runoff, due to their widespread distribution, toxicity, and elevated bioaccumulation.[4] Naphthalene exposure can cause hemolytic anemia, liver and kidney damage, neurological damage, and cataracts.[5,6] It is metabolized into alpha-naphthol, toxic to blood cells and organs. Anthracene is not acutely toxic, carcinogenic, or mutagenic, but may damage the hematopoietic system and lymphoid system, and cause skin allergy.[7,8]

PAHs get released into rainwater systems from highways, motorways, and other surfaces after a rainy event.[9] A considerable amount of municipal runoff is released directly, without treatment, into surface water sources such as lakes and rivers, causing risks to humans, fish, and other aquatic life.[10,11] As a result, it is deemed necessary to remove organic molecules from contaminated rainwater before dumping it into water reservoirs. PAHs are primarily consumed by humans through direct contact with polluted water, dietary consumption of PAH-containing food items, and inhalation.[12] PAHs are highly lipid-soluble, structurally complex, and stable compounds that can lead to inflammatory reactions, cancer, and teratogenic and reproductive disorders.[13] Epidemiological studies have shown that PAHs are the ninth most threatening compound to human health and the environment.

ANT and NAP are vital models for PAH degradation studies due to their structural similarities with carcinogenic and mutagenic PAHs like benzo(a)anthracene, benzo(a)pyrene, and benzo(a)naphthalene.[14] ANT and NAP are low molecular weight PAH compounds with high water solubility (Table 1), making them a potential water system contaminant.[15] The organic colloid of PAHs adsorbs and increases their concentration in aquatic systems, making them easy to transport through soil/sediment pores and end up in water reservoirs.[16] PAHs also

Table 1 Physiochemical properties of anthracene and naphthalene

Property description	Anthracene	Naphthalene
Mol. wt	178	128
Cas no.	120-12-7	91-20-3
M. Pt (°C)	215–219	78–80
B. Pt. (°C)	341	217
Vapor pressure (kPa)	0.01	0.93
Solubility (mg L^{-1})	0.64	31.6
$t_{1/2}$ (h)	17	8
Log P	4.56	3.34
Log Koc	4.8–6.8	
Environ. con. in runoff water (mg L^{-1})	16–1728	19–2510
Color	Colorless	White solid crystals/flakes
Odor	Weak aromatic	Strong odor of coal tar

Table 2 Rate constant and half-life values of anthracene (ANT) and naphthalene (NAP) with the photocatalysts under optimized conditions (p-values for fit < 0.05)[a]

Catalyst	NAP			ANT		
	k (h^1)	$t_{1/2}$ (min)	R^2	k (h^1)	$t_{1/2}$ (min)	R^2
Cu@ZnO	0.05544	12.1	0.98	0.05775	12.5	0.97
ZnO	0.0319	21.7	0.98	0.0294	23.5	0.96
Blank[b]	0.002	346.5	0.99	0.0018	385	0.99

[a] Note: triplicate experiments ($n = 3$) were evaluated to estimate the error bar. [b] Blank (15 mL of each pollutant with a definite concentration without a catalyst).

evaporate and are adsorbed onto soil particles and organic matter fractions, making removal from water components and other environmental matrices essential. These are carcinogenic even at low concentrations.[17] Their slow natural biodegradation and recalcitrant nature make them resistant to biological and chemical degradation.[18] This has impelled serious investigation for efficient remediation strategies for PAHs. In recent years, a growing number of studies have focused on the photocatalytic removal of PAHs from water samples, primarily employing heterogeneous photocatalysis exhibiting wide-ranging responses throughout the visible light spectrum.[19] Heterogeneous photocatalysis, as an effective low-cost technique, was used for removing PAHs from water through photodegradation with the assistance of different photocatalysts. Transition metal ion-doped semiconductor nanoparticles have proven to be good photocatalysts and have enhanced quantum efficiency compared to bulk forms.[20] Various nanomaterials such as Fe_2O_3@ MIL-101, ZnO, $CoFe_2O_{4-x}$, Ag and Cu, $CeVO_4$, $CdSe@TiO_2$, and many more which are listed in Table 2 are employed for the removal of NAP and ANT.[21–26] Extensive studies have been reported, in particular, on the catalytic properties of transition metal ion-doped semiconductor nanoparticles. Among the several photocatalysts (SnO_2, Fe_2O_3, SiO_2, and TiO_2), the nanoparticles of ZnO are well-known metal oxide nanoparticles.[27,28] It has distinctive physicochemical properties including sensitivity, stability, and high surface area. The use of ZnO is restricted due to the high band-gap (>3 eV) of ZnO and rapid e^-/h^+ pair recombination; these nanoparticles are sources of UV exposure and excitation. ZnO is the major dominating material used for photocatalysis causing the natural environment to become more bio-rich.[29,30] Hence to overcome such a problem, a possible approach to get over these restrictions, surface imperfections, bandgap moderation, and more probability of photogenerated e^-/h^+ recombination is by doping of ZnO nanoparticles with metals (Cu, Ag, and CO).[31–33] In ZnO : Cu^{2+}, interesting catalytic properties have been reported.[25] The current study aimed to prepare a novel sunlight-active green synthesized Cu doped ZnO (Cu@ZnO) nanocomposite by using the leaf extract of *Azadirachta indica* (neem) for the removal of NAP and ANT (Fig. 1). The juice from the leaves serves as reducing and capping agents for the synthesis of various types of nanoparticles. The leaf extract of *A. indica* was chosen for the production of nanoparticles due to its favorable performance,
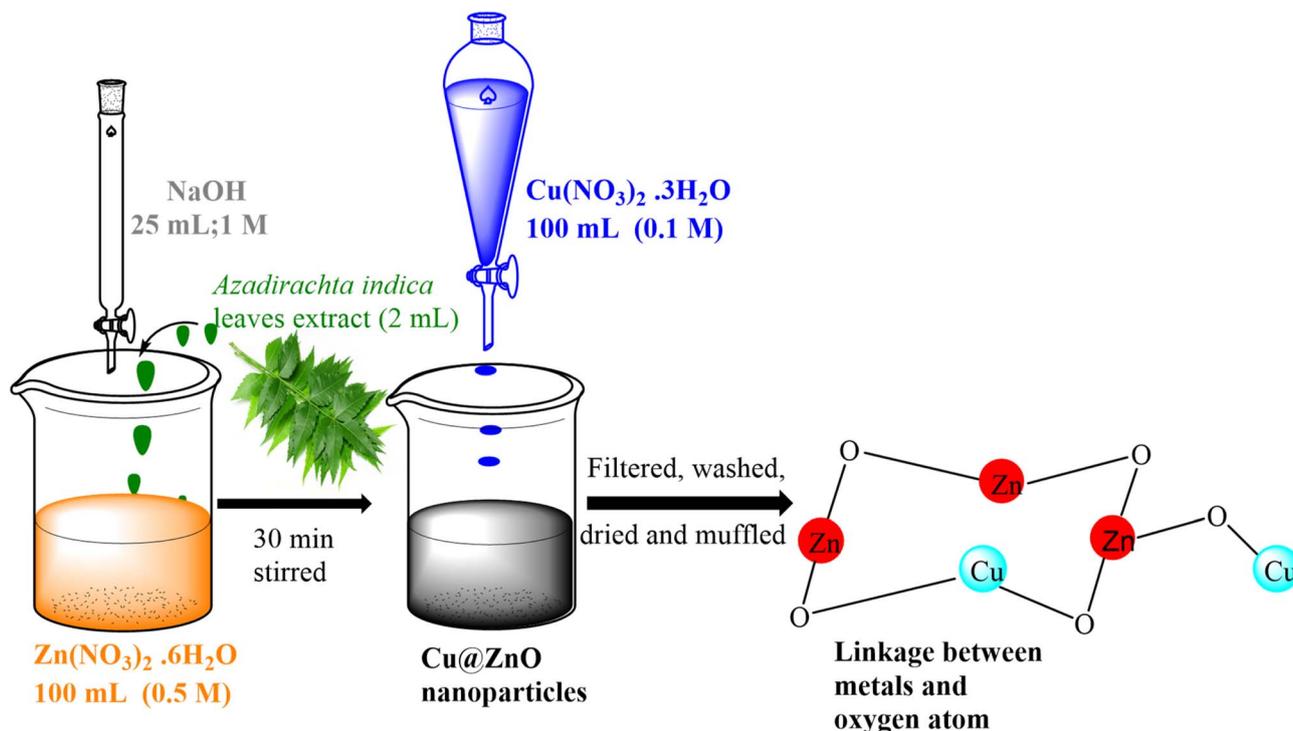
Fig. 1 Possible reaction mechanism for the formation of the Cu@ZnO nanocomposite in the presence of the *A. indica* leaf extract.

therapeutic benefits, and ease of availability in India.[34] Adsorption capacity and kinetics were investigated through batch tests using simulated rainwater, including the effect of PAH concentration, pH, and catalyst dose on removal efficiency. The role of free radicals, dissolved organic matter and inorganic ions during the degradation of PAHs by nanomaterials was evaluated by scavenger analysis, humic acid, and chloride ions, respectively. For establishing the sustainability, the reusability of the nanocomposite was investigated. Field-collected rainwater was used to confirm the catalytic performance of synthesized nanoparticles for the real system.

2. Experimental methodology

2.1. Materials

Zinc nitrate hexahydrate ($Zn(NO_3)_2\cdot 6H_2O$), sodium hydroxide (NaOH), sodium bicarbonate ($NaHCO_3$), and copper nitrate trihydrate ($Cu(NO_3)_2\cdot 3H_2O$) were purchased from Loba Chemie, India. Methanol and acetonitrile were purchased from Sigma (HPLC grade, 99.5%). Anthracene (ANT) and naphthalene (NAP) were purchased from Merk, India. The stock solution of both ANT and NAP was prepared in benzene. The whole experiment was conducted using deionized water as the solvent. The *A. indica* leaves used to make the plant extract were gathered nearby (MNIT Jaipur campus, India). Throughout the experiment, the temperature and solar intensity were measured using thermometers and pyranometers, respectively.

2.2. Preparation of the plant extract

Deionized water was used to wash and chop the *A. indica* leaves into smaller pieces. Nearly, 5 g of leaves were mixed with water,

crushed in a pestle and mortar, and then filtered. For synthesis, the PE solution was stored at 4 °C. Due to the leaves of *A. indica* being a significant source of quercetin-3-glucoside, galic acid, and polyhydroxy flavonoids, they also contain many polyphenols, and its extract was used as both the surfactant and reducing agent for nanoparticle synthesis. The presence of phenols (4.25 0.04%), flavonoids (7.43 0.03%), glycosides (0.11 0.01%), alkaloids (1.90 0.01%), tannins (0.86 0.02%) and saponins (2.50 0.01%), in the *A. indica* leaf extract further supported this fact. The interfacial tension was decreased by these phytochemicals to regulate particle development. Directly using biological extracts would be more effective since plant parts play a dominant role in the decrease of precursors. The aqueous extract of *A. indica* leaves acts as a capping as well reducing agent for the metal ions to produce metal nanoparticles.[35] The reduction of metal ions is carried out by polyols (such as polyphenols, flavonoids, and glycosides), which are oxidized to carbonyl functional group. The metallic ions were first reduced by polyphenols, flavonoids, and glycosides before being stabilized by their adhesion to the surface of the newly created nanoparticles. To regulate particle size, saponins and alkaloids decreased the likelihood of agglomeration.

2.3. Green synthesis of ZnO and the Cu@ZnO nanocomposite

2.3.1. ZnO nanoparticles. The solution of $Zn(NO_3)_2\cdot 6H_2O$ (0.1 M, 100 mL) was prepared in distilled water, and 2 mL *A. indica* leaf extract was added with regular stirring for 20 min. To obtain pH 9, a solution of NaOH (1 M, 25 mL) was then added dropwise and stirred for half an hour at room temperature. After this, the solution is left alone until a larger yield of precipitates

© 2024 The Author(s). Published by the Royal Society of Chemistry

Environ. Sci.: Adv., 2024, **3**, 249–265 | **251**

has been formed. The precipitates were dried for six hours at 60 °C followed by heat treatment at 300 ± 1 °C for 2 hours.

2.3.2. Cu@ZnO. An aqueous solution of $Cu(NO_3)_2 \cdot 3H_2O$ (0.1 M, 100 mL) was prepared and added to 100 mL suspension solution of ZnO nanoparticles (2.5 g) with continuous stirring for 40 min to get a homogenous mixture, and it was kept undisturbed overnight. The obtained grey-black precipitates were filtered, washed, dried at 60 °C, and subjected to heat treatment at 300 ± 1 °C for 2 hours. Fig. 1 describes the schematic representation of nanocomposite synthesis.

Through the use of instrumental methods, both synthesized nanomaterials were characterized. The details of instruments used for PXRD, FE-SEM, FT-IR, XPS, and band gap and zeta potential analysis were discussed in the ESI.†

2.4. Set up for the photocatalysis degradation of ANT and NAP by using a nanocomposite of Cu@ZnO from simulated rainwater (SRW)

To remove toxic PAHs from the SRW under sunlight irradiation, the photoactivity capabilities of the Cu@ZnO and ZnO nanoparticles were investigated. The stock solutions of both PAHs were prepared in benzene. To adjust the salinity of the simulated rainwater (SRW), the desired volume of 10 mM NaCl and 3 mM $NaHCO_3$ buffered solution was added to PAH stock solutions. The pH of the aqueous solution was adjusted to the desired pH with borax (0.1 M NaOH + 0.025 M of borax) and citrate buffer (0.1 M trisodium citrate + 0.1 M citric acid) as needed throughout the experiment. Other investigations also used salinity and buffer levels that were chosen to be reflective of standard rainwater conditions.[36] The amount of organic pollutants NAP and ANT (10–60 mg L^{-1}), photocatalytic dosage (2–12 mg), pH (3 to 9), and duration were optimized to achieve maximal removal. For 200 min (11 am to 2.20 pm), the stimulated samples were exposed to sunlight under optimal conditions. Throughout the experiment, the temperature and solar intensity were measured using pyrometers and thermometers, respectively. The average ambient conditions that were observed were 440 ± 183 lux and 30 ± 1.5, respectively. The reaction mixtures were also examined in complete darkness with nanocatalysts and sunlight without nanocatalysts to assess the impact of irradiation sources like adsorption and photolysis. The area ratio of the HPLC peak (at RT) and calibration equation are used to calculate the concentration of PAHs in the treated solution (Fig. 6a and b). Eq. 1, in which C_i is the pollutant's initial concentration and C_f is its final concentration, was used to compute the synthetic photocatalyst's percent degradation efficiency.

$$\% \ Degrdation = \frac{C_i - C_f}{C_i} \times 100 \qquad (Eq. \ 1)$$

3. Materials characterization

The details of instrumental and analysis conditions are discussed in the supplementary data (ESI) file.†

3.1. Crystallinity parameters and crystal structure analysis

The crystallinity, strain, composition, crystallite size, and crystal structure of nanomaterials were determined by PXRD analysis. Due to Cu doping into the ZnO lattice, the Cu@ZnO nanocomposite displayed crystalline behavior with an extra peak compared to ZnO spectra (Table 1S†). The (100), (002), (101), (200), (110), (103), and (112) planes at respective locations 31.8°, 34.4°, 36.3°, 47.6°, 56.7°, 62.9°, and 66.5° with the perfect agreement of ICSD card no. 01-079-2205 are shown in the ZnO spectra.[37] ZnO nanoparticles formed a hexagonal wurtzite crystal structure with $a = b = 3.3$ A°, $c = 5.9$ A°, and =90°, =120° (space group: $P6_3mc$). Cu doping caused additional peaks in the Cu@ZnO spectra at 44.2°, 49.7°, and 68.1° locations with the related planes (111), (102), and (200) (ICSD card no: 98-018-6303). Along with the $P6_3mc$ space group,[38] space no. 186 was observed in hexagonal Cu@ZnO with lattice parameters $a = b = 0.32$ nm; $c = 0.52$ nm and $\alpha = \beta = 90°$, and $\gamma = 120°$. The density and volume of Cu@ZnO nanoparticles were determined to be 5.69 g cm^{-3} and 47.42 × 10^6 pm,[3] respectively. The most strong and narrow peak is that of ZnO (101) with a d-spacing of 2.4 A° showing the decrease in peak intensity and the peak broadening, suggesting the Cu-doped ZnO crystal. Oxygen vacancies and lattice disorder induce peak widening.[31] The XRD peaks of Cu-doped ZnO samples also shift slightly toward a higher Bragg's angle indicating an increase in the lattice constant. The slight change in the lattice parameters and crystallite size suggests that the substitution of Cu ions into the Zn sites could occur. The crystallite size of ZnO (23.9 nm) and Cu@ZnO (21.3 nm) was calculated by Debye–Scherer's equation (eqn 1S);† eqn (2S) and (3S)† were used to calculate the lattice strain and dislocation density of nanomaterials. Crystallinity parameters (dislocation density and lattice strain) were reduced from ZnO (0.13%; 0.19 × 10^{-3}) to Cu@ ZnO (0.21%, 3.1 × 10^{-3}) due to Cu coupling, indicating improved amorphous behavior and doping. These variables influence structural flaws, which demonstrated the highest electron loss from vacancies in Cu@ZnO. Differences in crystallite size, lattice strain, and dislocation density revealed the doping of parent materials in the nanocomposite.[34] The presence of both ZnO and Cu peaks in the composites indicates that the Zn–O–Cu interaction was formed *via* strong interfacial contacts (Fig. 2a and c).

3.2. Spectral and molecular bonding analysis

The FT-IR analysis ranged between 400 and 4000 cm^{-1}, and the pellets were prepared by a combination of potassium bromide and a small amount of nanoparticles. Stretching frequencies of ZnO nanoparticles were 3470 cm^{-1}, 1109 cm^{-1}, and 490 cm^{-1}, signifying OH (due to surface acidity), Zn–O–Zn, and Zn–O stretching vibrations, respectively (Fig. 2b and d). The peaks at 2930 cm^{-1}, 1520 cm^{-1}, and 1425 cm^{-1} were caused by bending vibrations in the C–H and C–O stretching, and O–H bending caused by the presence of phytochemicals in the *A. Indica* leaf extract is utilized during nanomaterial fabrication (Table 2S†). Cu@ZnO spectra show additional peaks at 1115 cm^{-1}, and 435 cm^{-1} owing to Zn–O–Cu and Cu–O stretching, respectively,
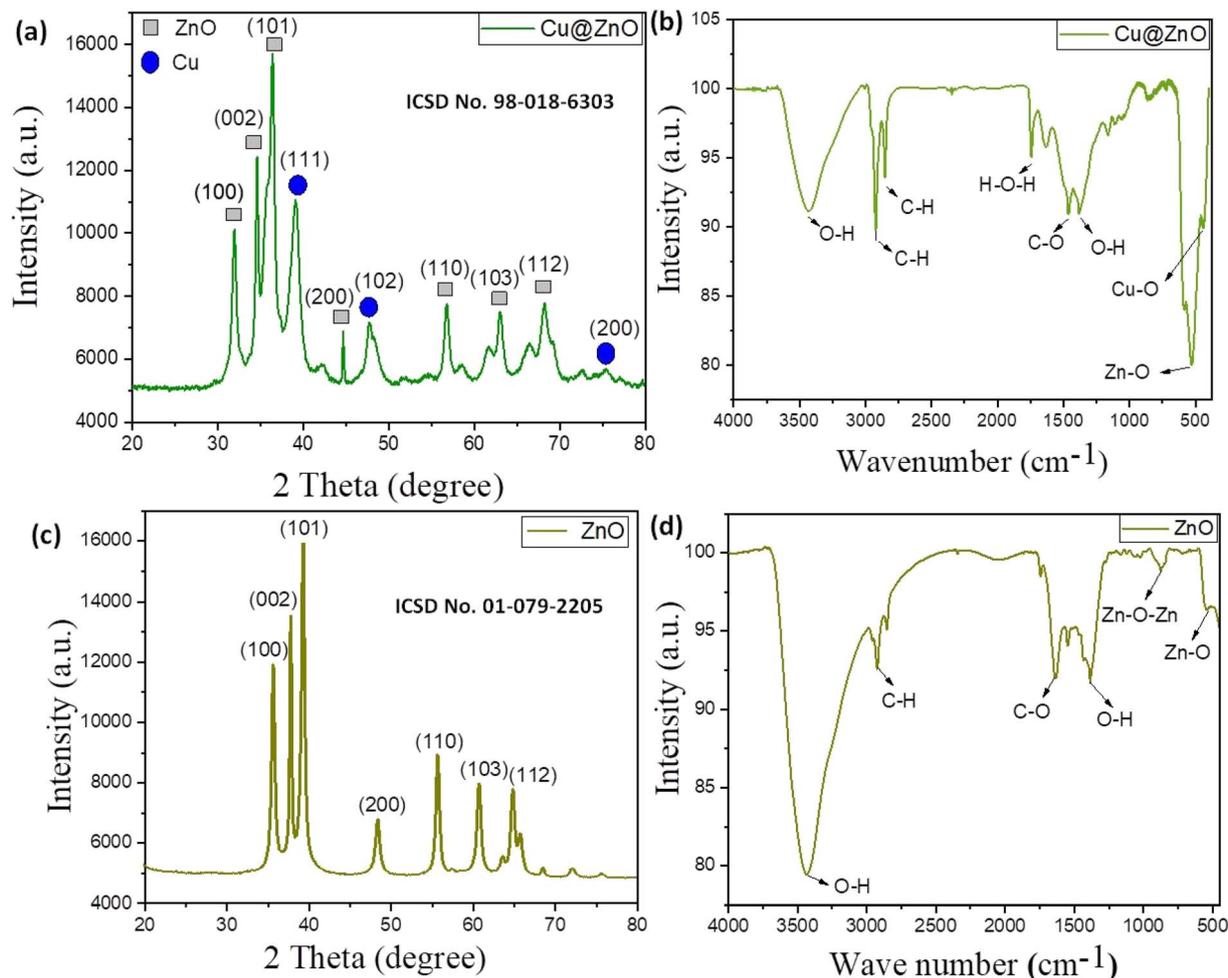
Fig. 2 (a) and (c) P-XRD patterns; (b) and (d) FT-IR spectra of Cu@ZnO and CuO nanoparticles, respectively.

demonstrating Cu doping with ZnO.[37] These findings and peak patterns were consistent with previous research. Peak shifting observed in Cu@ZnO nanocomposite spectra compared to parent spectra (ZnO) demonstrated efficient doping of both parent nanomaterials. The peak details corresponding to their vibration frequency are detailed in the ESI file.†

3.3. Morphology, crystallinity, and size distribution analysis

FE-SEM and HR-TEM techniques were used to analyze the surface morphology, particle size, and elemental content of the fabricated nanoparticles. Both ZnO (distorted nanoflower) and Cu@ZnO were found to have (accumulated nanospheres) average particle sizes smaller than 100 nm (Fig. 3a–e). The tiny spherical Cu particles embedded into ZnO pores formed with Cu@ZnO nanospherical cluster type morphology had smaller particle size (Fig. 2b). HR-TEM pictures of Cu@ZnO also revealed spherical particles with very small irregularly shaped particles. It was obvious that ZnO contributed far more than Cu, and the shape was altered as a result of the successful doping of ZnO with Cu. Energy dispersive spectroscopy (EDS) was also utilized to identify the elemental composition of Cu@ZnO, which included Zn (69.51%), Cu (9.11%), O (20.15%), and C (1.23%). The EDS spectrum of ZnO indicates 65.23% Zn and

34.77% Cu (Fig. 2Sa–e†). The presence of carbon and a larger proportion of oxygen in nanomaterial spectra might be attributed to phytochemicals contained in plant extracts.[27,34] The EDS data correlated well with the PXRD data of nanoparticles, indicating that the ZnO content of the Cu@ZnO nanocomposite was higher than that of Cu. HR-TEM SAED pattern HR-fringe examination revealed the interior shape and crystallinity of synthesized nanoparticles. The appearance of opaque concentric dots in a circular shadow of the Cu@ZnO nano-framework confirms the electron diffraction pattern and its semi-crystalline behavior (Fig. 2 (ii)). The molecular structure and size of Cu and ZnO, which have a substantial influence on the processes of aggregation, crystal formation, pre-nucleation, and nucleation, are responsible for the morphological difference.[34,37]

3.4. Surface and chemical composition analysis

The surface characteristics of synthesized nanomaterials were calculated using gas adsorption analysis and X-ray photoelectron spectroscopy (XPS). The research comprises the surface areas, pore sizes, and pore volumes determined using the N_2 adsorption/desorption isotherm model for all synthesized nanomaterials. A type IV isotherm and H3 hysteresis ring with
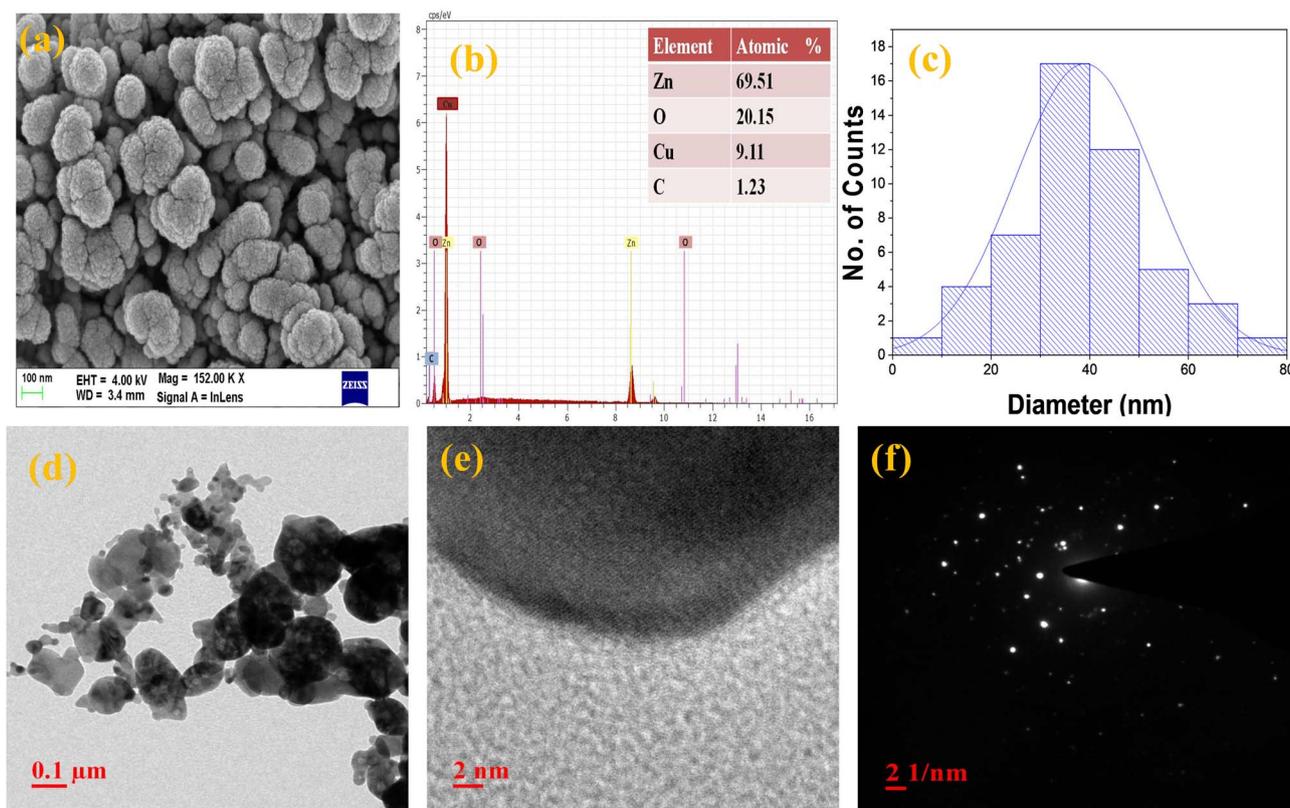
Fig. 3 (a) FE-SEM and (b) EDS with the atomic percentage, (c) size histogram, and (d) and (e) HR-TEM image with the (f) SAED pattern of the Cu@ZnO nanocomposite.

a relative pressure = 0.05–0.25 demonstrated the mesoporous structure of the nanocomposite with the greatest surface area (39.2 m^2 g^{-1}) followed by ZnO (16 m^2 g^{-1}).[39] The BJH model was used to compute the adsorption isotherm.[40] The BJH model confirmed the mesoporous shape of synthesized nanoparticles, and the average pore size followed the order of Cu@ZnO (1.9 nm) and ZnO (1.5 nm), which was consistent with the particle size found in the TEM examination. The substantial absorbing nature of Cu doped in ZnO enhances the overall results. Furthermore, it inhibits nanoparticle agglomeration and clumping. Greater surface area indicates greater light capture on the surface (Fig. 5a and b), which leads to improved photocatalytic efficiency of Cu@ZnO.[23]

Next, XPS spectra are used to study the chemical states of the Cu-doped ZnO sample (Fig. 4). The study used an Al Kα radiation source with 0.8 eV resolution power to study XPS spectra. The spectral analysis was conducted using CASA XPS software. The XPS spectrum of the Cu@ZnO nanocomposite revealed the presence of Zn (2p), Cu (2p), O (1s), and C(1s) with atomic percentages of 43.44%, 27.8%, 15.54%, 9.83%, and 1.94%, respectively (Fig. 4a–e). Due to traces of plant extract (phytochemicals), two deconvoluted carbon peaks with binding energies of 286.8 eV and 284 eV have been detected.[27] Moreover, two significant photoelectron components, 1022 eV and 1045 eV, ascribed to Zn 2p$_{3/2}$ and Zn 2p$_{1/2}$, respectively, were identified in the Zn 2p spectra of ZnO. The sharpness of Zn 2p$_{3/2}$ peaks further supports the +2 oxidation state of Zn in ZnO. The typical doublet of Cu^{2+} is

attributed to two primary XPS resolved peaks with the binding energy centered at 952 eV Cu(2p1$_{3/2}$) and 932 eV Cu(2p$_{3/2}$).[34] The asymmetric O1s peak was fitted by using three peaks with centers at 530 eV (O–Zn/O–Cu), 533 eV (O–C), and 531 (surface hydroxyl).[27] This interaction demonstrated that the formation of the Zn–O–Cu complex may be due to the transfer of electrons from Cu to ZnO. The XPS results show good co-relation with EDS data and confirmed the effective doping of ZnO and Cu.

3.5. Optical properties and stability analysis

The transitory energy levels of pure and Cu-doped ZnO NPs were determined using UV-visible spectroscopy. The band gap of the produced Cu@ZnO nanomaterials was estimated using UV-visible reflectance spectra (Fig. 5c). The assumption behind the Tauc equation is that energy is dependent on the absorption coefficient (α), as described in the ESI.† The results demonstrated the reduced band gap after doping Cu@ZnO: 2.3 eV, and ZnO: 3.4 eV. The synergistic effects and variable changes in adsorption caused by doping shifts the band gap in the visible region. A larger band gap of ZnO restricted the environmental application in the visible region.[41] Cu provides an extra energy level to the electron as a result of the life span of charged species (e$^-$/h$^+$) increasing, and their recombination is restricted. Thus Cu@ZnO nanoparticles may absorb more visible light and exhibit enhanced photocatalytic activity as compared to ZnO (Fig. 3Sc and d†). When the band gap narrows due to strain, the wavelength increases and shifts more into the visible region.[27]
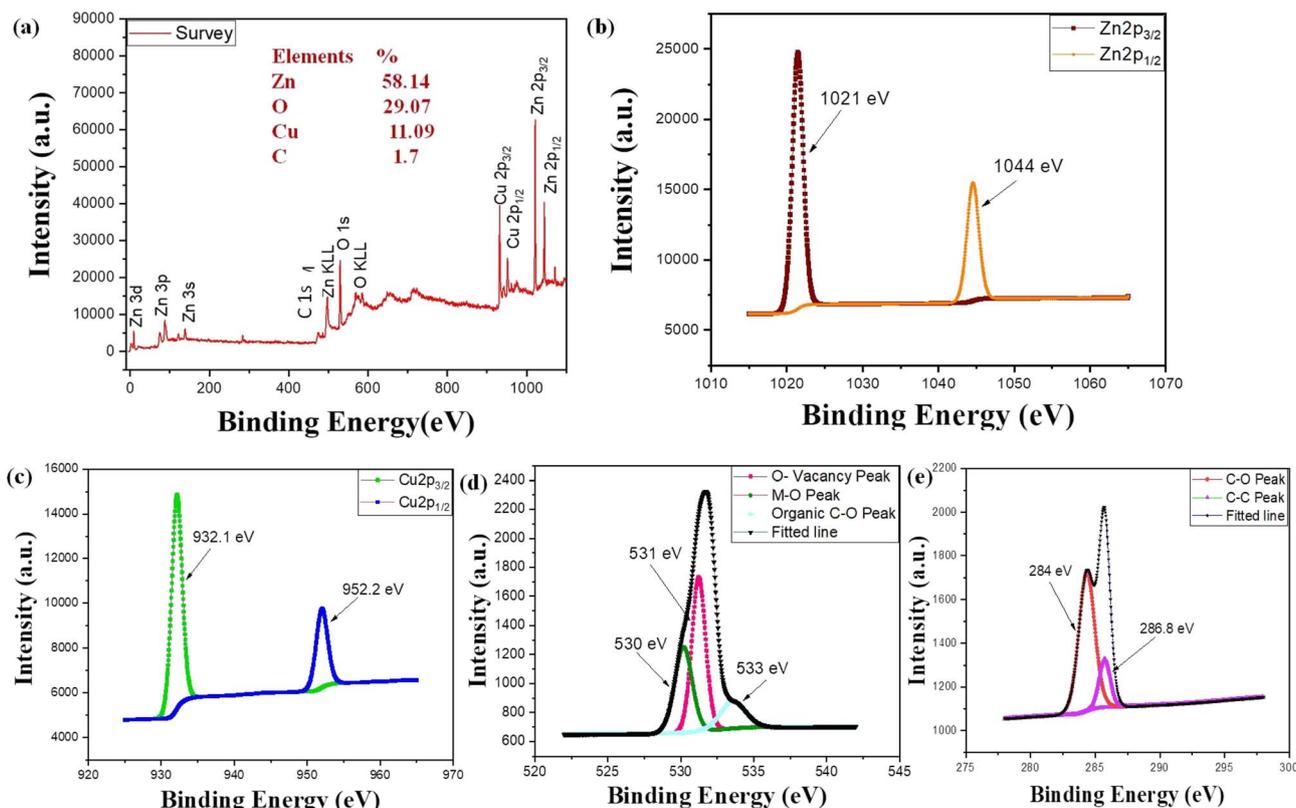
Fig. 4 (a) XPS elemental survey and (b) elemental profile of Zn, (c) Cu, (d) O and (e) C, respectively.

In the presence of Cu, such an electronic transition of ZnO NPs promoted the phenomenon of doping. When the UV-vis spectroscopy data were compared to the SEM data as shown in Fig. 3, it became obvious that the red shift in the optical gap is connected to the size of the nano-agglomerates. As the size of the nano-agglomerates increased and the electronic transition gaps shrunk, the optical absorption gradually redshifted.

To evaluate the stability and charge of the material, zeta potential analysis was employed. The zeta potential value for Cu@ZnO is −30.2 mV and ZnO is −15.7 mV (Fig. 3Sa and b†). To conduct zeta potential measurements, pH 7 was chosen because point zero charges (pzc) between 6.2 and 8 are stable for metal oxides and modified composites.[27,34] The more negative value of the particle size results from the probability of lesser agglomeration and stabilization of nanoparticles after doping. Similar results were also reported in the literature for the compounds CuO–NiHCF, Mn–CuO, ZnS–ZnO and Ag–ZnO.[39,41–43]

4. Optimization factor for photocatalytic degradation of ANT and NAP

The pollutant concentration (10–60 mg L^{-1}), photocatalyst dosage (2–12 mg), and pH (3–9) all affected the photocatalytic performance of the Cu@ZnO nanocomposite and ZnO nanoparticles used for the elimination of hazardous ANT and NAP

(Fig. 6a–c). The concentration of the contaminants was chosen based on their prevalence in the environment (soil: 330–20,000 ng g^{-1}; sediments: 809–7880 ng g^{-1}; water: 0.30 to 15 800 μg L^{-1}). Maximum pollutant removal (ANT and NAP) was reported in the presence of sunshine, at a pollutant concentration of 10 mg L^{-1}, a nanophotocatalyst quantity of 10 mg, and neutral pH. The decrease in percentage removal with increasing pollutant concentration is caused by too many pollutant molecules filling the limited area of the glass vials, requiring more active species. Furthermore, the ANT and NAP breakdown products might be utilizing fewer hydroxyl radicals. The amount of hydroxyl radicals in the reaction mixture was inadequate to eliminate a larger amount of hazardous pollutants. The addition of more active sites on nanocatalysts aided in the modification of ANT and NAP degradation by boosting the amount of photocatalyst to the appropriate scale. Later, as the number of nanocatalysts increased, the curve began to flatten because the nanocatalysts became inactive as a result of molecule collisions. In addition, the cause of nanoparticle accumulation and the screening effect restrict sunlight from reaching contaminating substances.[42,43] Consequently, it was found that when pollution concentrations grew, the efficiency of nanocomposite degradation reduced. The pH range (3–9) is also being studied since it significantly influences the removal of pollutants. The highest removal of ANT and NAP was seen at pH 7 due to the mechanism of ion screening and the photocatalyst's optimum permanence.[27,34] The effect of solar

© 2024 The Author(s). Published by the Royal Society of Chemistry

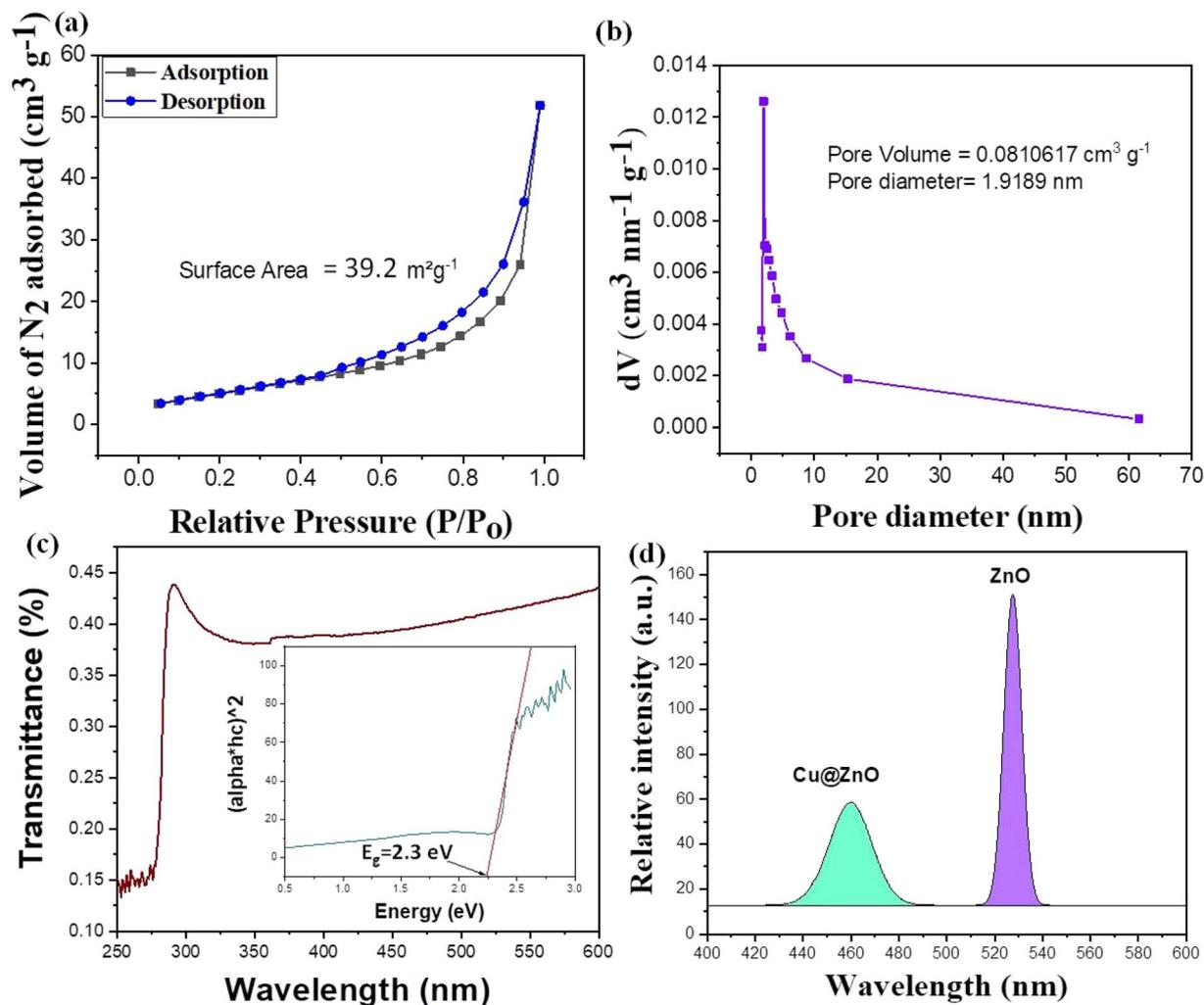*Environ. Sci.: Adv.*, 2024, **3**, 249–265 | **255**

Fig. 5   (a) Nitrogen adsorption (BET) isotherms, (b) BHJ plot, (c) UV-visible optical absorption spectrum and optical band gap (inset figure) and (d) photoluminescence (PL) spectrum of the Cu@ZnO nanocomposite.

irradiation on photocatalytic degradation is studied using a blank sample without catalysts (photolysis) and a dark sample (adsorption) under optimum conditions (Fig. 7a and b) (pollutant concentration: 10 mg L^{-1}; photocatalyst amount: 10 mg; pH 7). The elimination of both pollutants (ANT and NAP) by the photocatalyst was found to be greater in natural sunshine (79–96%), in the dark (30–65%), and photolysis (12–34%). The findings show that a sufficient number of nanoparticles focus on band-gap events that occur above the surface and excite charge carriers due to the adequate availability of energy in daylight.[39,42] Furthermore, decor with natural light exhibited the greatest pollutant degradation *via* energy transfer with a minimal band gap that targeted the perception area. Both contaminants are successfully removed from water by the Cu@ZnO nanocomposite and are degraded in the sun by photocatalysis. In addition, sunlight is less costly, safer, and simpler to access than UV sources, which may even degrade the catalyst and other contaminants.

4.1.   Effect of humic acid and scavenger analysis on photodegradation of ANT

Environmental water reservoirs consist of naturally organic materials, such as humic acid (HA), with quantities ranging from 0.1 to 20 mg L^{-1}.[27,42] It has been discovered that HA interacts with water treatment procedures to variable degrees; therefore, it is interesting to study the probable impact of HA on ANT breakdown by Cu@ZnO. The ANT degradation experiment used (2 mL; 0.1 and 1 M) HA to test the influence on the degradation of 10 mgL^{-1} ANT by Cu@ZnO. The graphs reveal that HA altered the ANT degradation profile. From the observation, when the amount of HA in solution increases, the degradation of ANT decreases, resulting in a lower degradation efficiency of nanocatalysts (Fig. 4Sa†). This behavior may be connected to HA's noted capacity to scavenge active oxidizing species ($^{\cdot}$OH and O$^{2-\cdot}$) and hence reduce their availability for ANT breakdown. Interestingly, the negative effects of HA on ANT degradation result in reduced active site accessibility for pollutant degradation, leading to lower photodegradation of
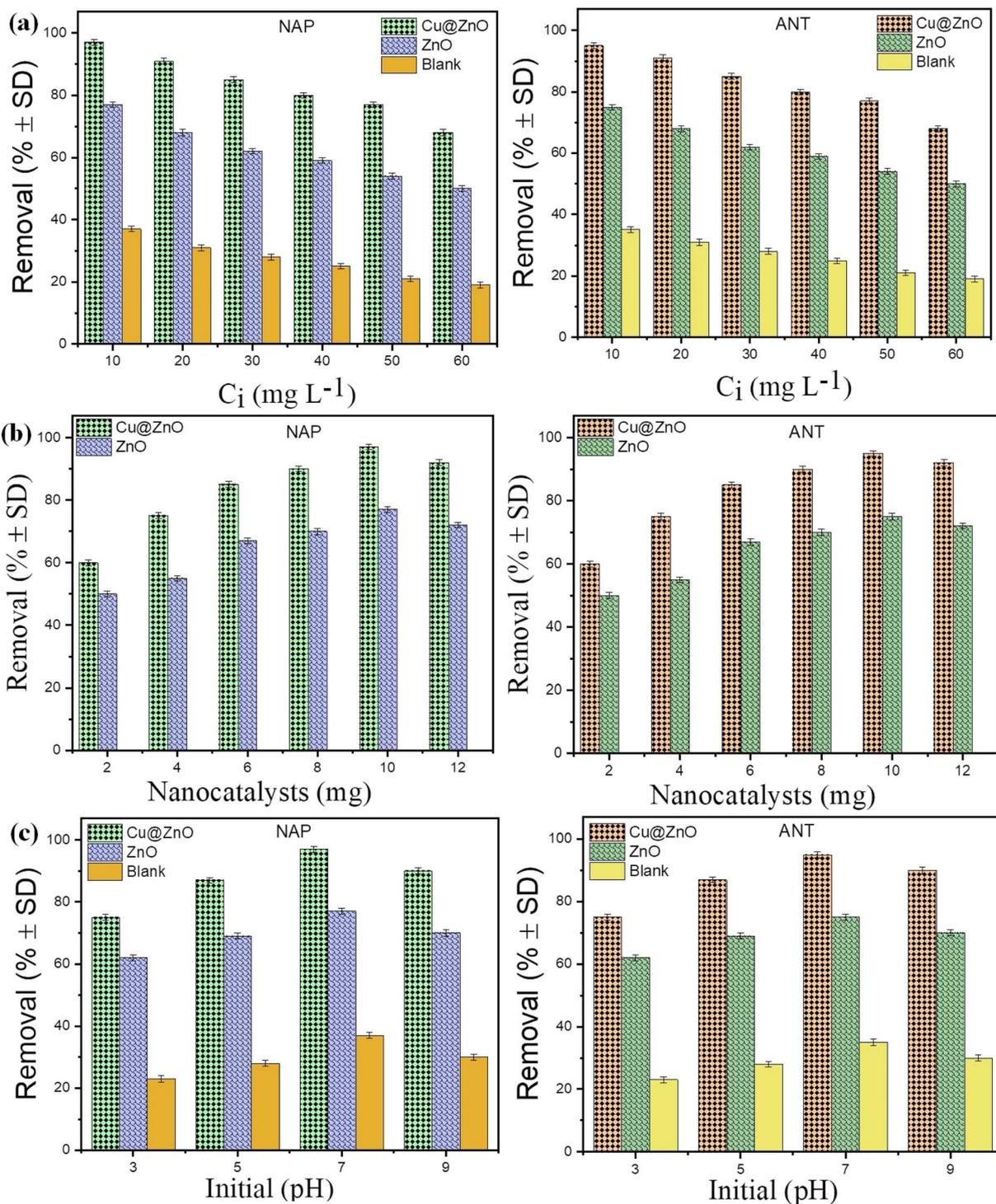
Fig. 6 Percentage degradation of PAHs on ZnO and Cu@ZnO nanocomposites at (a) different initial concentrations (10–60 mg L^{-1}), (b) nanocatalyst amounts (2–12 mg), and (c) initial pH (3–9). Note: ($n = 3$; triplicate used for result validation).

PAHs during SRW and sunshine exposure. In addition, the ANT degradation was somewhat influenced by the chloride ionic content, which varied between 0.01 and −0.10 mol L^{-1} (Fig. 4a). As the ionic concentration increased, the pace of the reaction slowed, and the efficiency of degradation reduced for the same inorganic ion. The competitiveness between the ions and ANT

for the Cu@ZnO accessible reaction sites may be responsible for this.

The ultimate goal of this investigation was to determine which reactive species are responsible for ANT and NAP degradation. The charge separation observed in the presence of sunshine is caused by the promotion of e$^-$ from lower to higher
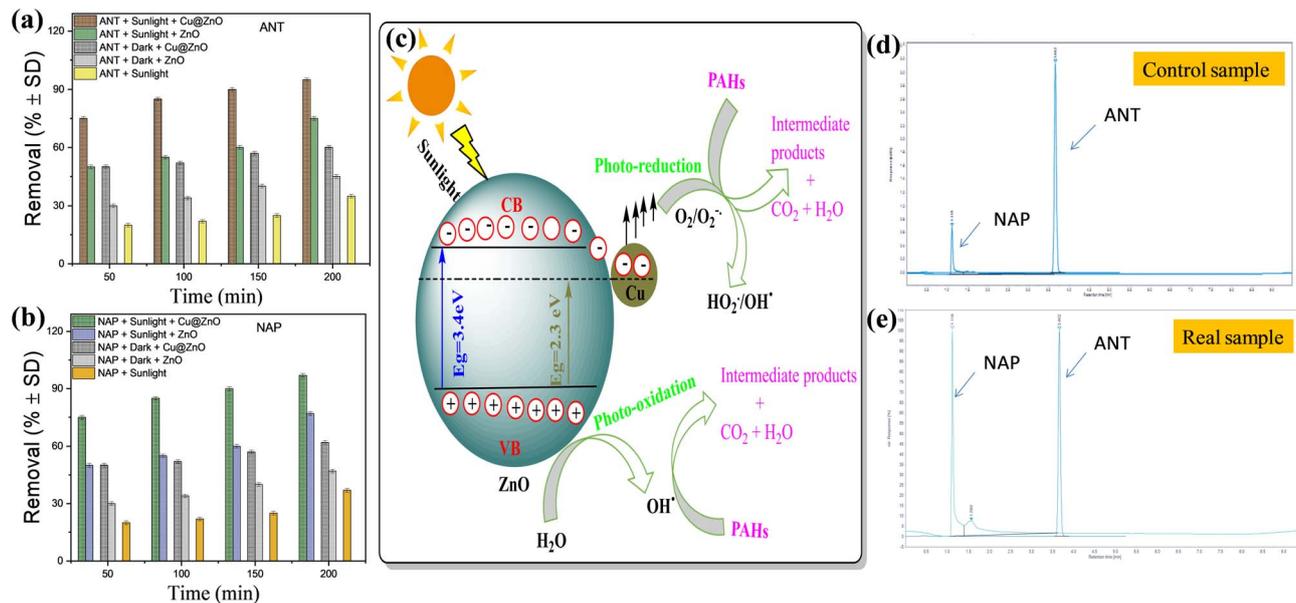
Fig. 7 Effect of the irradiation source on the degradation of (a) ANT and (b) NAP and (c) schematic representation of the charge separation mechanism for the degradation of PAHs over the Cu@ZnO nanocomposite; chromatogram for naphthalene and anthracene with mobile phase: ACN-MEOH (8 : 2); flow rate: 1.5 mL min; column temperature: 35 °C; UV detection (254 nm) for the (d) control sample and (e) real sample.

energy levels. As hydroxyl radicals formed when very active h^+ reacts with H_2O and $^\bullet O_2$ is produced when e^- interacts with dissolved O_2 molecules in water. Following this, the hydroperoxyl radical ($HO_2^\bullet$) is developed when O_2 reacts with H^+ and results in the emergence of a superoxide anion due to contact with $OH^\bullet$ radicals.[42] The reactive species that result in the breakdown of HBCD were discovered using t-BuOH and $CHCl_3$ as scavengers of $HO^\bullet$ and $O^{2-\bullet}$ radicals, respectively.[34] In a 250 mL conical flask containing 10 mg L^{-1} pollutant, a photocatalytic dosage (10 mg) at neutral pH (7), and 2 mL of quenchers, the conical was exposed to sunshine for 1 hour. As a control sample, an identical sample was made without any quencher compounds. As a result, superoxide ions ($O^{2-\bullet}$) and holes (h^+) play complementary roles in photocatalytic degradation, whereas the hydroxyl radical ($^\bullet OH$) is the dominating active species. The degradation rate of t-BuOH was the slowest, followed by $CHCl_3$ (Fig. 4Sb†). Nevertheless, Scavenger trapping research indicated that $HO^\bullet$ is mostly responsible for ANT elimination. The rate of degradation of ANT in the presence of various scavengers is shown in Fig. 8a and b. Other nanocomposite materials, such as ZnO, ZnO@NiO, ZnO@Bi$_2$O$_3$, Bi$_2$O$_3$@CdS, and CuO@NiHCF, exhibited similar findings, showing that hydroxyl radicals play an important role in the degradation of organic pollutants.[27,34,43]

4.2. Proposed kinetics and adsorption model of the removal of ANT and NAP

The Cu@ZnO nanocatalyst demonstrated rapid degradation of ANT (96%) and NAP (91%) under optimized conditions (pollutant concentration: 10 mgL^{-1}, nanocatalyst: 10 mg, pH 7, and sunshine) (Fig. 7a and b and 8c). When exposed to sunlight, electron excitation commences at the lower band gap of the Cu@ZnO nanocatalyst. The synergism phenomenon altered the

electron lifetime. Massive quantities of hydroxyl have been generated as a result of the oxidation of ANT and NAP (Fig. 7c). A huge number of electrons were generated during the process, resulting in the breakdown of harmful and carcinogenic pollutants into oxidant intermediate products and safer metabolites.[44–49] To describe the ANT and NAP adsorption phenomena, discrete adsorption models such as Langmuir, Freundlich, Dubinin–Radushkevich (DRK), Sips, and Temkin (Fig. 5S†) were used. The SI data comprise more details about adsorption model curves. For each adsorption model, the statistical value of p- and regression (R^2) value were computed, and it was demonstrated that the Langmuir isotherm was followed throughout the adsorption process for all adsorption models. On the other hand, the statistical validity of the DRK, Temkin, Slips, and Freundlich models was not proved. Table 2 includes the half-life ($t_{1/2}$) and rate constant (k^{-1}) of the parent nanomaterials and doped nanoparticles. Because all other adsorption models had insufficient statistical parameters and a negative slope value, for Cu@ZnO with the lowest $t^{1/2}$ and greatest k-value, the Langmuir model best fit the adsorption studies for the removal of both PAHs with nanocatalysts (Fig. 6Sa and b†). Table 1S† shows the statistical parameters (R^2 and p values) for ANT and NAP adsorption that are used to compare different isotherms. Cu@ZnO absorbed the greatest quantity of ANT and NAP, followed by ZnO nanoparticles (Table 3).

5. Photocatalytic degradation mechanism of ANT and NAP

The complete removal process is often divided into two steps: initial adsorption of pollutants on nanocatalyst surfaces, and then photocatalytic disintegration by reactive oxygen species generated by the semiconducting characteristics of

Paper

Environmental Science: Advances

Table 3 Comparative degradation studies of anthracene (ANT) and naphthalene (NAP) by nanoparticles[a]

Pollutant parameters	Reaction parameters	Removal efficiency	Ref.
ANT (100 mL; 0.025 mg L^{-1})	ZnO NPs (1 mg); reaction time = 240 min; light source = UV light photo reactor (368 nm by using 2 UV lamps, 20 W each)	96%	18
ANT (50 mL; 20 mg L^{-1})	Ni–TiO$_2$@C NPs (0.05 g); reaction time = 50 min; light source = visible light photo reactor (520 nm with 350 W power)	99.9%	44
ANT (100 mL; 25 mg L^{-1})	Ti$_2$O NPs (175 mg); reaction time = 22 days; light source = UV light photo reactor (308.15 K and 2.5 mW cm^{-2} of light intensity)	70%	45
ANT (10 mL; 2mg L^{-1})	NiO–ZnO NPs	98%	46
	ZnCo$_2$O$_4$ NPs	95%	
	MnCo$_2$O$_4$ NPs	92%	
	CoFe$_2$O$_4$ NPs (80 mg each); Reaction time = 12 h; light source = natural sunlight	88%	
ANT (100 mL; 50 mg L^{-1})	MgO-carbon NPs (6 g); reaction time = 60 min; light source = natural sunlight	96.05%	47
ANT (10 mL; 4 mg L^{-1})	Fe$_3$O$_4$/MIL-101 NPs (12.7 g), pH = 6, reaction time = 60 min	95%	48
Anthracene (2 mL; 50 mg L^{-1})	α-FeOOH and Fe$_3$O$_4$ NPs (0.1 g), pH = 9.7–10.6, reaction time = 10 hours; light source = UV irradiation (254 nm at ambient temperature)	90%	49
ANT (15 mL; 0.001 mg L^{-1})	CdSe@TiO$_2$ NPs (0.1 g); reaction time = 120 min; light source = visible light and monochromatic lights of 420, 450, 550, and 600 nm from a 500 W xenon arc lamp	100%	22
NAP (50 mL; 30 mg L^{-1})	La–N–TiO$_2$/AC NPs (and 0.01 g), Reaction time = 2 hours; light source = visible light irradiation (500 W Xe lamp; λ = 420 nm)	93.5%	50
NAP (100 mL; 50 mg L^{-1})	ZnO/Ag/GO NPs (500 mg g^{-1}), Reaction time = 20 min, light source = 250 W Xe lamp	85%	51
NAP (100 mL; 10 mg L^{-1})	WO$_3$-MWCNT NPs (2.5 g) nanocomposite, pH = 9, reaction time = 120 min. Light source = 570 W xenon lamp	—	52
NAP (500 mL; 10 mg L^{-1})	ZnO and Fe-doped ZnO NPs (100 mg), pH = 9, reaction time = 240 min. Light source = Uv light (16 W at 200–700 nm)	92.3%	53
NAP (50 mL; 50 mg L^{-1})	ZnO NPs (80 mg), reaction time = 120 min (30 °C, 280 V). Sonicator reactor was operated at a frequency of 20 kHz and a maximum power dissipation of 260 W	87.5%	54
NAP (0.004 mL; 50 mg L^{-1})	Ti^{3+} self-doped Fe$_2$O$_3$/TiO$_2$ NPs (0.053 g), reaction time = 15 hours; light source = solar light simulator (xenon lamp (500 W m^{-2})	90%	55
NAP (500 mL; 40 mg L^{-1})	Fe-doped ZnO NP (4 g) nanofibers, pH = 9, reaction time = 120 min; light source = UV light (16 W at 200–700 nm)	96%	56
NAP (50 mL; 10 mg L^{-1})	Co$_3$O$_4$/Bi$_2$O$_2$CO$_3$ NPs (25 mg); reaction time = 150 min; light source = 500 W xenon lamp, 400 nm	91.02%	57
NAP (200 mL; 30 mg L^{-1})	CeVO4 NPs (0.05 g); reaction time = 12 hours. Light source = solar light simulator Xe lamp (300 W)	95.1%	58
NAP (100 mL; 30 mg L^{-1})	FeMn/bio-char NPs (2 g); reaction time = 148 min; light source = 300 W xenon lamp, 400 nm	82.2%	59
NAP (10 mL; 7 mg L^{-1})	Ag and Cu NPs (5 mg) Reaction time = 30 min	98.81% (Cu) 89.71% (Ag)	20
ANT and NAP (100 mL; 10 mg L^{-1})	Cu@ZnO and ZnO (10 mg); pH = 7	ANT (89–94%)	Present study
	Reaction time = 120 min; light source = natural sunlight	NAP (90–96%)	

[a] Abbreviations: PAHs = polyaromatic hydrocarbons; ANT = anthracene; NAP = naphthalene; NPs = nanoparticles.

nanocatalysts.[50–52] The adsorption capacity of nanoparticles was increased by Cu doping due to the large surface area, which also allowed for the rapid transfer of ANT and NAP molecules to active sites. The valence (VB) and conduction (CB) band gap energies of photocatalysts are equivalent to or greater than that of the photons absorbed by the photocatalytic materials. Photon absorption causes charge separation by excitation of electrons from the VB to the CB and the subsequent formation of positive h$^+$ in the VB (Fig. 7c). In this study, the lifespan of

active species carrying charge influenced the photocatalytic breakdown of ANT and NAP. The decreased intensity of the nanocomposite in photoluminescence (PL) spectra avoids charge recombination (Fig. 5d). Lower PL emission intensity resulted in better charge carrier separation and quicker transit. The capacity of the Cu@ZnO nanocomposite to recombine electron and hole pairs was lowered due to inadequate intensity monitoring. Copper provides an extra level for the localization of excited or generated electrons from the ZnO CB and increases
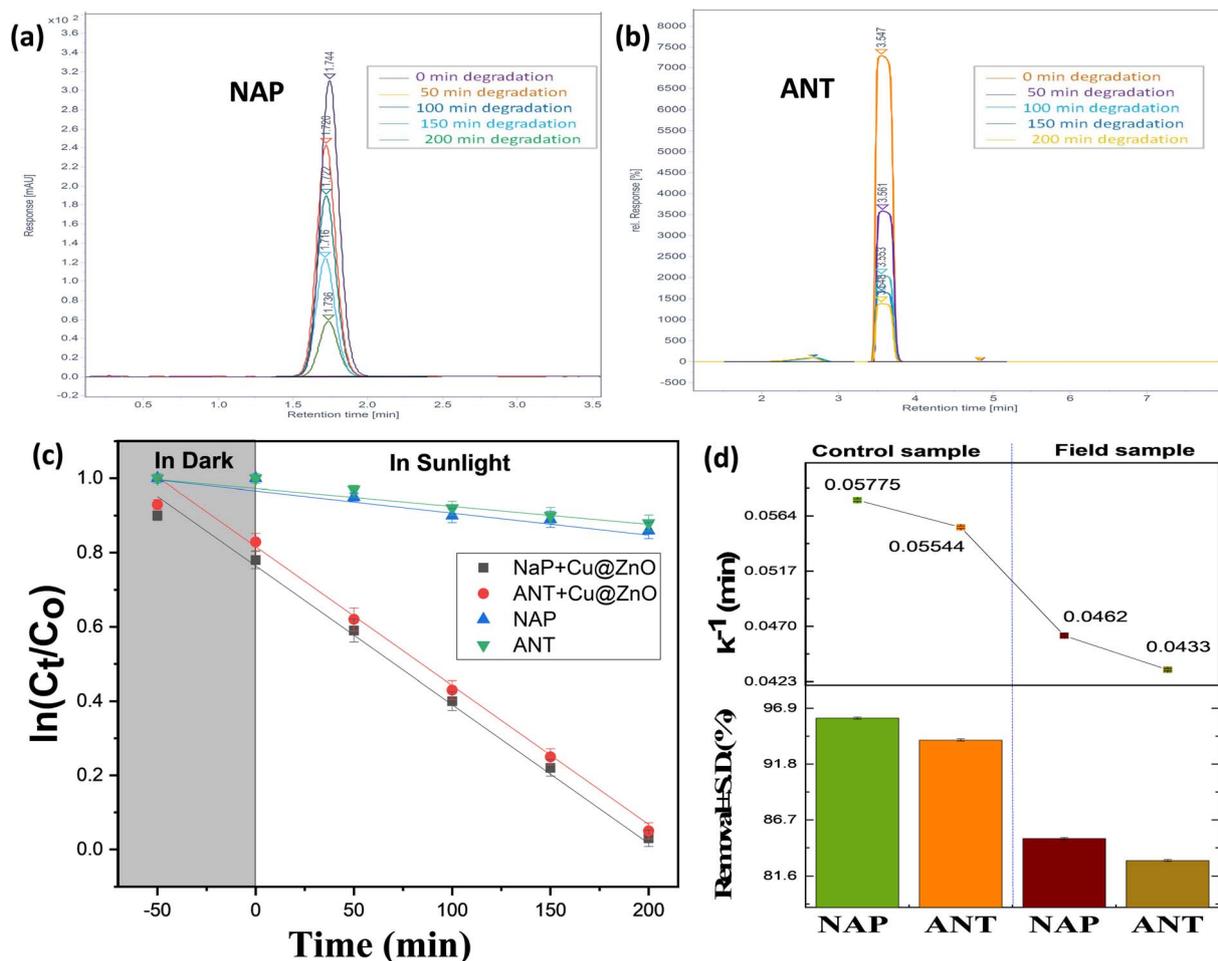
© 2024 The Author(s). Published by the Royal Society of Chemistry

Environ. Sci.: Adv., 2024, **3**, 249–265 | 259

Fig. 8 Chromatogram for (a) naphthalene and (b) anthracene with the mobile phase: ACN–MEOH (8 : 2); flow rate: 1.5 mL min; column temperature: 35 °C; UV detection (254 nm). (c) Reaction kinetics of the control sample and (d) removal efficacy with a rate constant of real and control samples over the Cu@ZnO nanocomposite.

the life span as well as shifts the adsorption of light toward the visible region, and can quickly accept electrons, whereas ZnO has a high electron density and can rapidly give electrons. ZnO (n-type) and Cu came into contact, which resulted in an increase in resistivity, a decrease in the number of n-type donor carriers, and a decrease in charge recombination.[31,35] Doping ZnO broadens the charged separation range, reducing e^-/h^+ recombination (Fig. 7c). The details of the photocatalysis degradation mechanism of ANT and NAP by Cu@ZnO are discussed in the ESI.†

6. Photodegradation pathways of NAP and ANT by using Cu@ZnO

For the sample of NAP and ANT (concentration: 10 mgL^{-1}, photocatalyst amount: 10 mg, neutral pH) in a 200 min degradation period, the liquid chromatography-mass spectrometer (GC-MS) technique was used. The total ion chromatogram (TIC) and mass spectra of degraded ANT and NAP are shown in Fig. 7S.† According to the suggested process for degradation depicted in Fig. 9a, hydroxyl radicals are responsible for breaking the complex structure

of toxic NAP and ANT into harmless and smaller metabolites. Anthracene-9,10-diol ($m/z = 210.1$) was produced as a result of the OH radical attacking the 9 and 10 sites of ANT during the photocatalysis process.[46] Anthracene-9,10-diol was immediately converted into 4,9-dihyroanthracen-9,10-dione ($m/z = 210.1$) which later degraded into oxidative products such as 3,hydroxyl-2,3-dihyronapthalene-2carboxylic acid ($m/z = 177.1$) and phthalic acid ($m/z = 166$). Similarly, the oxidation of NAP into naphthalene 1,2-diol by hydroxyl radicals attacks the aromatic ring (Fig. 9b). As the OH˙ radicals are present in huge amounts, hence, the free radical species again attack, and breakage of the C–C bond takes place resulting in 4-hydroxybenzoic acid ($m/z = 138$). Further oxidation of these compounds leads to the products oxalic acid ($m/z = 90$), acrylic acid ($m/z = 72$), and 2-propanol ($m/z = 58$),[45,47] and finally, breakage into safer metabolite products like CO_2 and H_2O.

7. Detection and removal of PAHs from a real rainwater sample

To investigate the practical potential of Cu@ZnO for photocatalytic removal of PAHS in real rain wastewater samples, the
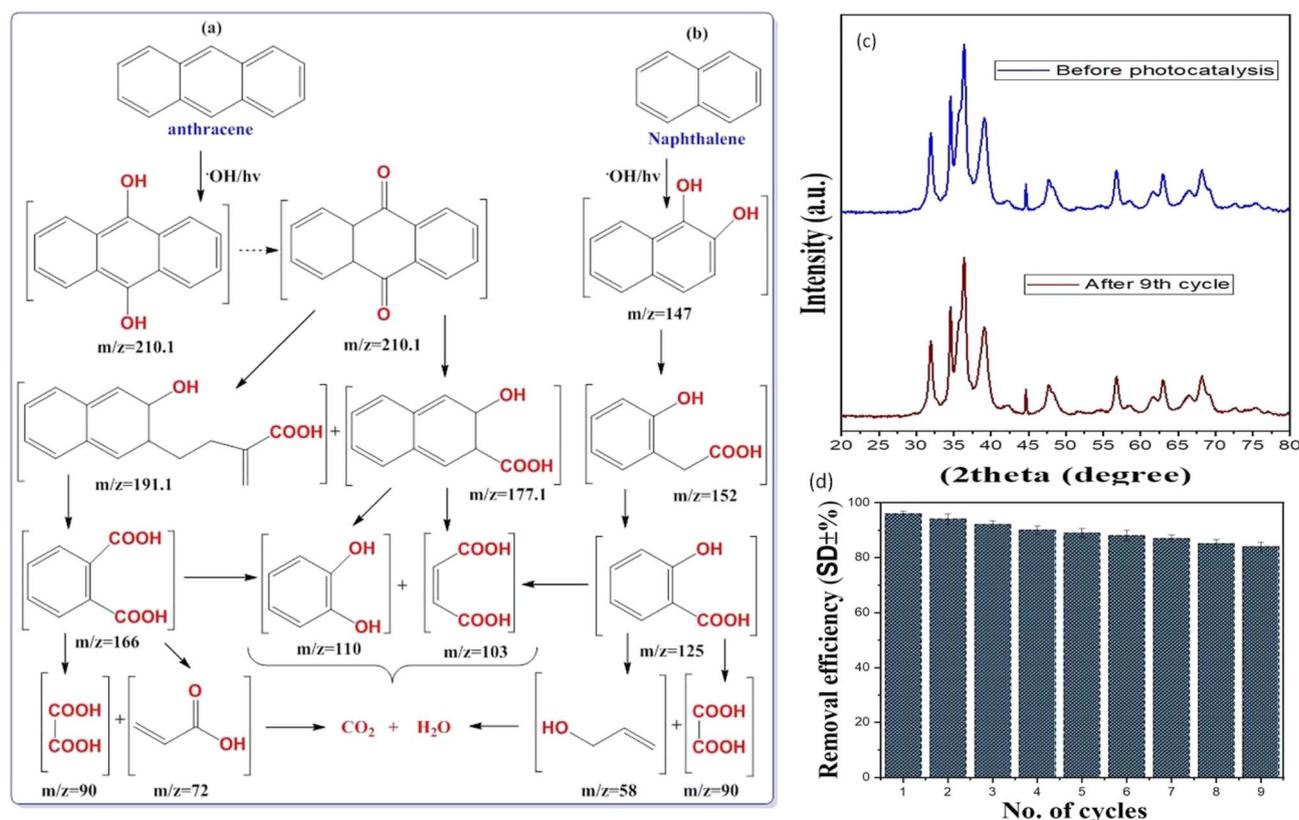
260 | Environ. Sci.: Adv., 2024, 3, 249–265

© 2024 The Author(s). Published by the Royal Society of Chemistry

Fig. 9 Proposed degradation pathway for the degradation of (a) ANT and (b) NAP and (c) XRD pattern and (d) reusability analysis up to the 9th cycle (triplicate for error bar) of the Cu@ZnO nanocomposite (concentration; 10 mg L^{-1}; pH = 7; nanocatalyst dose: 10 mg; natural sunlight exposure = 200 min).

rain wastewater sample (RWWS) was collected from two different time intervals from June to July (RWWS) from the vicinity of the Malaviya Nager, Jaipur, inlet to the way to the wastewater treatment plant. 1000 mL of each RWWS was collected in plastic bottles used for distilled water in the laboratory. ANT and NAT are common components of petroleum and diesel used in automobiles.[48] As a result of the usage of vehicles for transportation in everyday life activities, ANT and NAP have been identified in the RWWS. Table 4S† consists of the properties of the RWWS. The occurrences of PAHs in the RWWS were also detected by other research groups.[49,50] The collected water sample is centrifuged to remove impurities followed by liquid extraction to concentrate the PAHs and analysis by HPLC. The existence of ANT and NAP was verified by the appearance of peaks in the RWWS HPLC cromatogram at RT 3.5 min and 1.74 nm (Fig. 6d and e). The examination of actual rainfall sample degradation under ideal circumstances, wherein RWWS control PAHs samples degrade at their fastest rate during the day at the same intervals. The absorbance of ANT and NAP was suppressed and (84.2–82.9) % removal of PAHs was observed in 200 min (Fig. 6c and d). The comparative decline in the removal efficacy of the real sample compared to the control is caused by two factors: (i) the number of active species is limited according to catalyst dose, which removes both PAHs simultaneously; and (ii) the sample may contains other pollutants (PAHs, heavy metals, and pesticides) despite

the NAP and ANT, which further suggests the effectiveness of nanocatalysts.[51–58] Hence, the Cu@ZnO photocatalyst proved to be an efficient sunlight-active catalyst for real samples.

8. Comparison of degradation studies with the literature and recyclability performance of the photocatalyst

To determine the relative effectiveness of Cu@ZnO for NAP and ANT degradation in wastewater, a comparison of the current Cu@ZnO nanocomposite with other nanomaterials was conducted.[59–64] Table 2 displays the comparison findings. When compared to other nanomaterials in the literature, the present Cu@ZnO nanocomposite shows comparatively high degrading activity with considerable reusability for NAP and ANT degradation. To test the reusability of the catalysts (10 mg), new samples are centrifuged, washed with distilled water and solvent (acetone), and placed in a hot air oven for 6–7 hours. The efficiency of the Cu@ZnO nanocomposite was studied only for the ANT sample which declined from ANT: 96% to 85% after the 9th cycle showing effective reusability (Fig. 9b and c). The modest decrease in the percentage elimination of ANT in each successive run might be attributable to the nanomaterial recovery methods produced by adhesion within nanoparticles. A conglomerate nanoparticle's surface may also be coated with ANT, which would prevent the

major active positions for absorption of photons from functioning.[65–67] Thus hybrid nanocatalysts were found to be recyclable for the same return reaction scenario at least nine times while retaining catalytic activity and continuing to produce active species. Up until nine runs, Cu@ZnO nanocomposites were used with justification, according to the PXRD spectrum (Fig. 9b). After the nine cycles, however, the deterioration rate dropped to 89%. This is due to Cu@ZnO photo-corrosion and a minor degree of nanoparticle loss during centrifugal recycling. These two experiments proved that the catalyst could be recycled throughout the reaction. Thus, the Cu@ZnO nanocomposite could be a potential photocatalyst for the degradation of PAHs and other pollutants in wastewater.

9. Conclusion

The leaf extract of *A. indica was* employed for the synthesis of the photoactive catalyst Cu@ZnO nanocomposite by using a facile and eco-friendly methodology. The presence of both ZnO and Cu in the PXRD and FT-IR spectra of the Cu@ZnO nanocomposite confirmed effective doping with no impurities. The higher negative zeta potential value (-30.2 eV), lower band gap (2.3 eV), and high surface area (39.2 m^2 g^{-1}) of the Cu@ZnO nanocomposite showed good photo catalytic activity of PAH removal from the control as well as real rainwater in daylight. Maximum removal observed under sunlight as in the dark with optimized parameters and photocatalysis follows first-order kinetic models. Copper provides an extra level for the localization of excited or generated electrons from the ZnO CB and increases the life span as well as shifts the adsorption of light toward the visible region and can quickly accept electrons, whereas ZnO has a high electron density and can rapidly give electrons. ZnO (n-type) and Cu came into contact, which resulted in an increase in resistivity, a decrease in the number of n-type donor carriers, and a decrease in charge recombination. Additionally, in the presence of sunlight due to $e^{-}-h^{+}$ pairs large amounts of HO$^{\bullet}$ species are produced in water and attack the more feasible site of toxic pollutants (ANT and NAP) to convert them into safer metabolites, as confirmed by GC-MS studies. The real-life application of the green fabricated Cu@ZnO nanocomposite was also investigated in a real rainwater sample. Furthermore, to emphasize the concept of sustainability, the Cu@ZnO nanocomposite was reusable up to 9 times. Overall, the Cu@ZnO nanocomposite is a potential alternative material that might be used in practical applications and is anticipated to lessen environmental stress due to its good stability and reusability.

Conflicts of interest

There are no conflicts to declare.

Acknowledgements

References

1 H. I. Abdel-Shafy and M. S. Mansour, A review on polycyclic aromatic hydrocarbons: source, environmental impact, effect on human health and remediation, *Egypt. J. Pet.*, 2016, **25**(1), 107–123, DOI: **10.1016/j.ejpe.2015.03.011**.

2 G. M. Fernandes, D. A. Martins, R. P. Dos Santos, I. S. de Santiago, L. S. Nascimento, A. H. Oliveira, F. Y. Yamamoto and R. M. Cavalcante, Levels, source appointment, and ecological risk of petroleum hydrocarbons in tropical coastal ecosystems (northeast Brazil): Baseline for future monitoring programmes of an oil spill area, *Environ. Pollut.*, 2022, **296**, 118709, DOI: **10.1016/j.envpol.2021.118709**.

3 F. C. S. Lopes, C. Maria da Graça, P. Bargiela, H. S. Ferreira and C. A. D. M. Pires, Ag/TiO$_2$ photocatalyst immobilized onto modified natural fibers for photodegradation of anthracene, *Chem. Eng. Sci.*, 2020, **227**, 115939, DOI: **10.1016/j.ces.2020.115939**.

4 E. Azah, H. Kim and T. Townsend, Assessment of direct exposure and leaching risk from PAHs in roadway and stormwater system residuals, *Sci. Total Environ.*, 2017, **609**, 58–67, DOI: **10.1016/j.scitotenv.2017.07.136**.

5 S. Stohs, S. Ohia and D. Bagchi, Naphthalene toxicity and antioxidant nutrients, *Toxicology*, 2002, **180**, 97–105, DOI: **10.1016/S0300-483X(02)00384-0**.

6 S. Nayak and L. Patnaik, Histopathological and Biochemical Changes in the Gills of Anabas testudineus on Exposure to Polycyclic Aromatic Hydrocarbon Naphthalene, *Appl. Biochem. Biotechnol.*, 2023, **195**, 2414–2431, DOI: **10.1007/s12010-022-04214-x**.

7 J. L. Bonnet, P. Guiraud, M. Dusser, M. Kadri, J. Laffosse, R. Steiman and J. Bohatier, Assessment of anthracene toxicity toward environmental eukaryotic microorganisms: Tetrahymena pyriformis and selected micromycetes, *Ecotoxicol. Environ. Saf.*, 2005, **60**, 87–100, DOI: **10.1016/j.ecoenv.2003.10.001**.

8 M. S. Goutam and M. A. Kumar, Anthracene Removal from Wastewater Using Biotechnological Interventions, in *Advanced and Innovative Approaches of Environmental Biotechnology in Industrial Wastewater Treatment*, Springer Nature Singapore, Singapore, 2023, pp. 443–454, DOI: DOI: **10.1007/978-981-99-2598-8_20**.

9 H. M. Hwang and G. D. Foster, Characterization of polycyclic aromatic hydrocarbons in urban stormwater runoff flowing into the tidal Anacostia River, Washington, DC, USA, *Environ. Pollut.*, 2006, **140**(3), 416–426, DOI: **10.1016/j.envpol.2005.08.003**.

10 M. W. Mullowney, C. H. Hwang, A. G. Newsome, X. Wei, U. Tanouye, B. Wan, S. Carlson, N. J. Barranis, E. Ó hAinmhire, W. L. Chen and K. Krishnamoorthy, Diaza-anthracene antibiotics from a freshwater-derived

262 | *Environ. Sci.: Adv.*, 2024, **3**, 249–265

© 2024 The Author(s). Published by the Royal Society of Chemistry

actinomycete with selective antibacterial activity toward Mycobacterium tuberculosis, *ACS Infect. Dis.*, 2015, **1**(4), 168–174, DOI: **10.1021/acsinfecdis.5b00005**.

11 G. Mallesham, S. Balaiah, M. A. Reddy, B. Sridhar, P. Singh, R. Srivastava, K. Bhanuprakash and V. J. Rao, Design and synthesis of novel anthracene derivatives as n-type emitters for electroluminescent devices: a combined experimental and DFT study, *Photochem. Photobiol. Sci.*, 2014, **13**, 342–357, DOI: **10.1039/c3pp50284h**.

12 X. Duan, G. Shen, H. Yang, J. Tian, F. Wei, J. Gong and J. J. Zhang, Dietary intake polycyclic aromatic hydrocarbons (PAHs) and associated cancer risk in a cohort of Chinese urban adults: Inter-and intra-individual variability, *Chemosphere*, 2016, **144**, 2469–2475, DOI: **10.1016/j.chemosphere.2015.11.019**.

13 A. Thacharodi, S. Hassan, T. A. Hegde, D. D. Thacharodi, K. Brindhadevi and A. Pugazhendhi, Water a major source of endocrine-disrupting chemicals: An overview on the occurrence, implications on human health and bioremediation strategies, *Environ. Res.*, 2023, **231**, 116097, DOI: **10.1016/j.envres.2023.116097**.

14 A. Kumari, V. Upadhyay and S. Kumar, A critical insight into occurrence and fate of polycyclic aromatic hydrocarbons and their green remediation approaches, *Chemosphere*, 2023, **329**, 138579, DOI: **10.1016/j.chemosphere.2023.138579**.

15 H. Tian, C. Li, Z. Wang, S. Zhao, Y. Xu and S. Wang, Polycyclic aromatic hydrocarbons degradation mechanisms in methods using activated persulfate: Radical and non-radical pathways, *Chem. Eng. J.*, 2023, **473**, 145319, DOI: **10.1016/j.cej.2023.145319**.

16 S. Bolan, L. P. Padhye, C. N. Mulligan, E. R. Alonso, R. Saint-Fort, *et al.*, Surfactant-enhanced mobilization of persistent organic pollutants: potential for soil and sediment remediation and unintended consequences, *J. Hazard. Mater.*, 2023, **443**, 130189, DOI: **10.1016/j.jhazmat.2022.130189**.

17 M. T. Alcántara, J. Gómez, M. Pazos and M. A. Sanromán, Combined treatment of PAHs contaminated soils using the sequence extraction with surfactant–electrochemical degradation, *Chemosphere*, 2008, **70**(8), 1438–1444, DOI: **10.1016/j.chemosphere.2007.08.070**.

18 S. Barathi, J. Gitanjali, G. Rathinasamy, N. Sabapathi, K. N. Aruljothi, J. Lee and S. Kandasamy, Recent trends in polycyclic aromatic hydrocarbons pollution distribution and counteracting bio-remediation strategies, *Chemosphere*, 2023, **337**, 139396, DOI: **10.1016/j.chemosphere.2023**.

19 F. C. Monteiro, I. D. L. Guimaraes, P. de Almeida Rodrigues, J. V. D. A. de Pinho and C. A. Conte-Junior, Degradation of PAHs using TiO$_2$ as a semiconductor in the heterogeneous photocatalysis process: A systematic review, *J. Photochem. Photobiol., A*, 2023, **437**, 114497, DOI: **10.1016/j.jphotochem.2022.114497**.

20 S. C. Zhu and F. X. Xiao, Transition Metal Chalcogenides Quantum Dots: Emerging Building Blocks toward Solar-to-Hydrogen Conversion, *ACS Catal.*, 2023, **13**, 7269–7309, DOI: **10.1016/j.jenvman.2023.118614**.

21 A. Tirado-Guizar, W. González-Gómez, G. Pina-Luis, J. T. E. Galindo and F. Paraguay-Delgado, Anthracene removal from water samples using a composite based on metal-organic-frameworks (MIL-101) and magnetic nanoparticles (Fe$_3$O$_4$), *Nanotechnol*, 2020, **31**(19), 195707, DOI: **10.1088/1361-6528/ab70fd**.

22 S. S. Hassan, W. I. El Azab, H. R. Ali and M. S. Mansour, Green synthesis and characterization of ZnO nanoparticles for photocatalytic degradation of anthracene, *Adv. Nat. Sci.: Nanosci. Nanotechnol.*, 2015, **6**(4), 045012, DOI: **10.1088/2043-6262/6/4/045012**.

23 X. Bai, W. Song, X. Ling, L. Guo, D. Hao and X. Zhang, Metal ion endogenous cycles of CoFe$_2$O$_{4-x}$ induced boosted photocatalytic/PMS degradation toward polycyclic aromatic hydrocarbons, *Nanoscale*, 2023, **15**(16), 7352–7364, DOI: **10.1039/D3NR00727H**.

24 S. Abbas, S. Nasreen, A. Haroon and M. A. Ashraf, Synthesis of silver and copper nanoparticles from plants and application as adsorbents for naphthalene decontamination, *Saudi J. Biol. Sci.*, 2020, **27**(4), 1016–1023, DOI: **10.1016/j.sjbs.2020.02.011**.

25 G. Lu, B. Song, Z. Li, H. Liang and X. Zou, Photocatalytic degradation of naphthalene on CeVO4 nanoparticles under visible light, *Chem. Eng. J.*, 2020, **402**, 125645, DOI: **10.1016/j.cej.2020.125645**.

26 L. Yang, S. Luo, R. Liu, Q. Cai, Y. Xiao, S. Liu, F. Su and L. Wen, Fabrication of CdSe nanoparticles sensitized long TiO2 nanotube arrays for photocatalytic degradation of anthracene-9-carbonxylic acid under green monochromatic light, *J. Phys. Chem. C*, 2010, **114**(11), 4783–4789, DOI: **10.1021/jp910489h**.

27 M. Rani, J. Yadav, S. Chaudhary and U. Shanker, An updated review on synthetic approaches of green nanomaterials and their application for removal of water pollutants: Current challenges, assessment and future perspectives, *J. Environ. Chem. Eng.*, 2021, **9**(6), 106763, DOI: **10.1016/j.inoche.2022.110246**.

28 N. M. Hosny, I. Gomaa, M. G. Elmahgary and M. A. Ibrahim, ZnO doped C: Facile synthesis, characterization and photocatalytic degradation of dyes, *Sci. Rep.*, 2023, **13**, 14173, DOI: **10.1038/s41598-023-41106-4**.

29 E. Benrezgua, B. Deghfel, A. Zoukel, W. J. Basirun, R. Amari, et al., Synthesis and properties of copper doped zinc oxide thin films by sol-gel, spin coating and dipping: A characterization review, *J. Mol. Struct.*, 2022, **1267**, 133639, DOI: **10.1016/j.molstruc.2022.133639**.

30 F. El-Sayed, M. S. Hussien, T. H. AlAbdulaal, A. Ismail, H. Y. Zahran, I. S. Yahia, M. S. Abdel-wahab, Y. Khairy, T. E. Ali and M. A. Ibrahim, Comparative Degradation Studies of Carmine Dye by Photocatalysis and Photoelectrochemical Oxidation Processes in the Presence of Graphene/N-Doped ZnO Nanostructures, *Crystals*, 2022, **12**, 535, DOI: **10.3390/cryst12040535**.

31 M. K. Gora, A. Kumar, S. Kumar, J. Nehra, B. L. Choudhary, *et al.*, The study of optical, structural and magnetic properties of Cu-doped ZnO nanoparticles, *J. Mater. Sci.:*

© 2024 The Author(s). Published by the Royal Society of Chemistry

Environ. Sci.: Adv., 2024, **3**, 249–265 | 263

Mater. Electron., 2023, **34**(4), 288, DOI: **10.1007/s10854-022-09713-5**.

32 M. I. Mohammed, R. M. Khafagy, M. S. Hussien, G. B. Sakr, M. A. Ibrahim, I. S. Yahia and H. Y. Zahran, Enhancing the structural, optical, electrical, properties and photocatalytic applications of ZnO/PMMA nanocomposite membranes: Towards multifunctional membranes, *J. Mater. Sci.: Mater. Electron.*, 2022, **33**, 1977–2002, DOI: **10.1007/s10854-021-07402-3**.

33 F. El-Sayed, M. S. Hussien, M. I. Mohammed, V. Ganesh, T. H. AlAbdulaal, H. Y. Zahran, I. S. Yahia, H. H. Hegazy, M. S. Abdel-Wahab, M. Shkir and S. Valarasu, The photocatalytic performance of Nd2O3 doped CuO nanoparticles with enhanced methylene blue degradation: synthesis, characterization and comparative study, *Nanomaterials*, 2022, **12**, 1060, DOI: **10.3390/nano12071060**.

34 M. Rani, Meenu and U. Shanker, Efficient cleanup of emerging contaminants by green biosynthesized Z-scheme-type Bi₂O₃@CdS nanocomposite with improved photoactivity, *Nanotechnol. Environ. Eng.*, 2023, **8**(1), 197–218, DOI: **10.1007/s41204-022-00283-9**.

35 H. Genç-Fuhrman, P. S. Mikkelsen and A. Ledin, Simultaneous removal of As, Cd, Cr, Cu, Ni and Zn from stormwater using high-efficiency industrial sorbents: Effect of pH, contact time and humic acid, *Sci. Total Environ.*, 2016, **566**, 76–85, DOI: **10.1016/j.scitotenv.2016.04.210**.

36 J. E. Grebel, J. A. Charbonnet and D. L. Sedlak, Oxidation of organic contaminants by manganese oxide geomedia for passive urban stormwater treatment systems, *Water Res.*, 2016, **88**, 481–491, DOI: **10.1016/j.watres.2015.10.019**.

37 M. Mittal, M. Sharma and O. P. Pandey, UV–Visible light induced photocatalytic studies of Cu doped ZnO nanoparticles prepared by co-precipitation method, *Sol. Energy*, 2014, **110**, 386–397, DOI: **10.1016/j.solener.2014.09.026**.

38 C. B. Ong, L. Y. Ng and A. W. Mohammad, A review of ZnO nanoparticles as solar photocatalysts: Synthesis, mechanisms and applications, *Renewable Sustainable Energy Rev.*, 2018, **81**, 536–551, DOI: **10.1016/j.rser.2017.08.020**.

39 V. Poliukhova, S. Khan, Z. Qiaohong, J. Zhang, D. Kim, S. Kim and S. H. Cho, ZnS/ZnO nanosheets obtained by thermal treatment of ZnS/ethylenediamine as a Z-scheme photocatalyst for H₂ generation and Cr (VI) reduction, *Appl. Surf. Sci.*, 2022, **575**, 151773, DOI: **10.1016/j.apsusc.2021.151773**.

40 D. Raoufi, Synthesis and microstructural properties of ZnO nanoparticles prepared by precipitation method, *Renewable Energy*, 2013, **50**, 932–937, DOI: **10.1016/j.renene.2012.08.076**.

41 P. S. Vindhya and V. T. Kavitha, Leaf extract-mediated synthesis of Mn-doped CuO nanoparticles for antimicrobial, antioxidant and photocatalytic applications, *Chem. Pap.*, 2023, **77**(5), 2407–2424, DOI: **10.1007/s11696-022-02631-0**.

42 M. R. Meenu and U. Shanker, Efficient photocatalytic degradation of bisphenol A by green synthesized CuO decorated nickel hexacyanoferrate nanocomposite, *Water Environ. J.*, 2023, **37**(3), 428–444, DOI: **10.1111/wej.12847**.

43 V. Vinitha, M. Preeyanghaa, M. Anbarasu, B. Neppolian and V. Sivamurugan, Chemical recycling of polyester textile wastes using silver-doped zinc oxide nanoparticles: an economical solution for circular economy, *Environ. Sci. Pollut. Res.*, 2023, **30**, 1–16, DOI: **10.1007/s11356-023-27567-0**.

44 S. Babel, P. A. Sekartaji and H. Sudrajat, ZnO nanoparticles for photodegradation of humic acid in water, *Environ. Sci. Pollut. Res.*, 2021, **28**, 31163–31173, DOI: **10.1007/s11356-021-12977-9**.

45 K. M. Mohamed, J. J. Benitto, J. J. Vijaya and M. Bououdina, Recent Advances in ZnO-Based Nanostructures for the Photocatalytic Degradation of Hazardous, Non-Biodegradable Medicines, *Crystals*, 2023, **13**(2), 329, DOI: **10.3390/cryst13020329**.

46 B. L. Martínez-Vargas, M. Cruz-Ramírez, J. A. Díaz-Real, J. L. Rodríguez-López, F. J. Bacame-Valenzuela, R. O. Borges, Y. O. Vidal, L. O. Frade, *et al.*, Synthesis and characterization of n-ZnO/p-MnO nanocomposites for the photocatalytic degradation of anthracene, *J. Photochem. Photobiol., A*, 2019, **369**, 85–96, DOI: **10.1016/j.jphotochem.2018.10.010**.

47 K. Mondal, S. Bhattacharyya and A. Sharma, Photocatalytic degradation of naphthalene by electrospun mesoporous carbon-doped anatase TiO₂ nanofiber mats, *Ind. Eng. Chem. Res.*, 2014, **53**(49), 18900–18909, DOI: **10.1021/ie5025744**.

48 M. Saeedi, L. Y. Li and M. Salmanzadeh, Heavy metals and polycyclic aromatic hydrocarbons: pollution and ecological risk assessment in street dust of Tehran, *J. Hazard. Mater.*, 2012, **227**, 9–17, DOI: **10.1016/j.jhazmat.2012.04.047**.

49 B. Guzel, Temporal variations and source identification of polycyclic aromatic hydrocarbons (PAHs) in rainwater collected in a semi-urban area within an industrial area in Turkey, *Polycyclic Aromat. Compd.*, 2022, **42**(8), 4965–4983, DOI: **10.1080/10406638.2021.1922467**.

50 M. Walaszek, P. Bois, J. Laurent, E. Lenormand and A. Wanko, Micropollutants removal and storage efficiencies in urban stormwater constructed wetland, *Sci. Total Environ.*, 2018, **645**, 854–864, DOI: **10.1016/j.scitotenv.2018.07.156**.

51 J. G. Langeveld, J. Post, K. F. Makris, B. Palsma, M. Kuiper and E. Liefting, Monitoring organic micropollutants in stormwater runoff with the method of fingerprinting, *Water Res.*, 2023, **235**, 119883, DOI: **10.1016/j.watres.2023.119883**.

52 M. Baruah, S. L. Ezung, S. Sharma, U. B. Sinha and D. Sinha, Synthesis and characterization of Ni-doped TiO₂ activated carbon nanocomposite for the photocatalytic degradation of anthracene, *Inorg. Chem. Commun.*, 2022, **144**, 109905, DOI: **10.1016/j.inoche.2022.109905**.

53 F. F. Karam, F. H. Hussein, S. J. Baqir, A. F. Halbus, R. Dillert and D. Bahnemann, Photocatalytic degradation of anthracene in closed system reactor, *Int. J. Photoenergy*, 2014, **2014**, 503825, DOI: **10.1155/2014/503825**.

54 M. Rani and U. Shanker, Mineralization of carcinogenic anthracene and phenanthrene by sunlight active bimetallic oxides nanocomposites, *J. Colloid Interface Sci.*, 2019, **555**, 676–688, DOI: **10.1016/j.jcis.2019.08.016**.

55 J. A. Kumar, D. J. Amarnath, S. A. Jabasingh, P. S. Kumar, K. V. Anand, *et al.*, One pot Green Synthesis of Nano magnesium oxide-carbon composite: Preparation, characterization and application towards anthracene adsorption, *J. Cleaner Prod.*, 2019, **237**, 117691, DOI: **10.1016/j.jclepro.2019.117691**.

56 A. Tirado-Guizar, W. González-Gómez, G. Pina-Luis, J. T. E. Galindo and F. Paraguay-Delgado, Anthracene removal from water samples using a composite based on metal-organic-frameworks (MIL-101) and magnetic nanoparticles (Fe_3O_4), *Nanotechnol*, 2020, **31**(19), 195707, DOI: **10.1088/1361-6528/ab70fd**.

57 H. Gupta, R. Kumar, H. S. Park and B. H. Jeon, Photocatalytic efficiency of iron oxide nanoparticles for the degradation of priority pollutant anthracene, *Geosyst. Eng.*, 2017, **20**(1), 21–27, DOI: **10.1080/12269328.2016.1218302**.

58 D. Liu, Z. Wu, F. Tian, B. C. Ye and Y. Tong, Synthesis of N and La co-doped TiO_2/AC photocatalyst by microwave irradiation for the photocatalytic degradation of naphthalene, *J. Alloys Compd.*, 2016, **676**, 489–498, DOI: **10.1016/j.jallcom.2016.03.124**.

59 N. Mukwevho, R. Gusain, E. Fosso-Kankeu, N. Kumar, F. Waanders and S. S. Ray, Removal of naphthalene from simulated wastewater through adsorption-photodegradation by ZnO/Ag/GO nanocomposite, *J. Ind. Eng. Chem.*, 2020, **81**, 393–404, DOI: **10.1016/j.jiec.2019.09.030**.

60 M. Farhadian, P. Sangpour and G. Hosseinzadeh, Preparation and photocatalytic activity of WO 3–MWCNT nanocomposite for degradation of naphthalene under visible light irradiation, *RSC Adv.*, 2016, **6**(45), 39063–39073, DOI: **10.1039/C6RA04642H**.

61 H. Muthukumar, A. Gire, M. Kumari and M. Manickam, Biogenic synthesis of nano-biomaterial for toxic naphthalene photocatalytic degradation optimization and kinetics studies, *Int. Biodeterior. Biodegrad.*, 2017, **119**, 587–594, DOI: **10.1166/jbns.2017.1422**.

62 S. Suresh, P. Kumari, J. M. Jha, S. Verma, S. Arisutha and P. N. Lens, Sonocatalytic removal of naphthalene from an aqueous solution using ZnO nanoparticles, *Aqua Water Infrastruct. Ecosyst. Soc.*, 2022, **71**(9), 1002–1015, DOI: **10.2166/aqua.2022.042**.

63 M. Sayed, B. Ren, A. M. Ali, A. Al-Anazi, M. N. Nadagouda, A. A. Ismail and D. D. Dionysiou, Solar light induced photocatalytic activation of peroxymonosulfate by ultra-thin Ti^{3+} self-doped Fe_2O_3/TiO_2 nanoflakes for the degradation of naphthalene, *Appl. Catal., B*, 2022, **315**, 121532, DOI: **10.1016/j.apcatb.2022.121532**.

64 A. D. Sekar, H. Muthukumar, N. I. Chandrasekaran and M. Matheswaran, Photocatalytic degradation of naphthalene using calcined FeZnO/PVA nanofibers, *Chemosphere*, 2018, **205**, 610–617, DOI: **10.1016/j.chemosphere.2018.04.131**.

65 Y. Guo, Y. Dai, W. Zhao, H. Li, B. Xu and C. Sun, Highly efficient photocatalytic degradation of naphthalene by Co_3O_4/$Bi_2O_2CO_3$ under visible light: A novel p–n heterojunction nanocomposite with nanocrystals/lotus-leaf-like nanosheets structure, *Appl. Catal., B*, 2018, **237**, 273–287.

66 G. Lu, B. Song, Z. Li, H. Liang and X. Zou, Photocatalytic degradation of naphthalene on $CeVO_4$ nanoparticles under visible light, *Chem. Eng. J.*, 2020, **402**, 125645, DOI: **10.1016/j.cej.2020.125645**.

67 L. Li, C. Lai, F. Huang, M. Cheng, G. Zeng, D. Huang, B. Li, S. Liu, M. Zhang, L. Qin and M. Li, Degradation of naphthalene with magnetic bio-char activate hydrogen peroxide: synergism of bio-char and Fe–Mn binary oxides, *Water Res.*, 2019, **160**, 238–248, DOI: **10.1016/j.watres.2019.05.081**.

© 2024 The Author(s). Published by the Royal Society of Chemistry

Environ. Sci.: Adv., 2024, **3**, 249–265 | **265**